Journal of Applied Polymer Science

WILEY

Applied Polymer SCIENCE

RESEARCH ARTICLE OPEN ACCESS

4D Printing of Composite Thermoplastic Elastomers for Super-Stretchable Soft Artificial Muscles

Abbas Bayati[1] | Davood Rahmatabadi[1] | Mahdi Khajepour[1] | Majid Baniassadi[1] | Karen Abrinia[1] | Mahdi Bodaghi[2] | Mostafa Baghani[1]

[1]School of Mechanical Engineering, College of Engineering, University of Tehran, Tehran, Iran | [2]Department of Engineering, School of Science and Technology, Nottingham Trent University, Nottingham, UK

Correspondence: Mahdi Bodaghi (mahdi.bodaghi@ntu.ac.uk) | Mostafa Baghani (baghani@ut.ac.ir)

Received: 8 January 2025 | **Revised:** 17 March 2025 | **Accepted:** 4 April 2025

Funding: The authors received no specific funding for this work.

Keywords: 4D printing | artificial muscles | carbon black | elastomers | nanocomposites

ABSTRACT

This study explores the development of soft, super-stretchable artificial muscles by 4D printing of composite thermoplastic elastomers. A propylene-based elastomer, combined with carbon black (CB) nanoparticles, is utilized to develop nanocomposite elastomers with enhanced mechanical properties. A pellet-based material extrusion technique is employed to overcome the challenges of filament buckling in traditional filament-based printing methods. The pure elastomer exhibits an elongation at break of 4048% and a tensile strength of 3.71 MPa, while the optimal nanocomposite (2% CB) achieves an elongation of 2665% and a tensile strength of 5.58 MPa. Scanning electron microscopy confirms that high-quality printing with well-bonded layers is achievable. The shape memory properties of printed elastomers are assessed through cyclic tests. It demonstrates the material's ability to recover its original shape after deformation with a drop in mechanical properties after each cycle controllable by CB reinforcements. Innovative artificial muscles are inspired by the chameleon's tongue, achieving significant strain recovery and lifting capabilities. Objects with varying weights are lifted by these muscles, showcasing potential for soft robotics and actuators. The potential of 4D printed composite elastomers in creating highly stretchable, efficient artificial muscles is highlighted, offering promising applications in fields requiring high elasticity and mechanical performance.

1 | Introduction

Artificial muscles are a diverse group of actuators that, like natural muscles, can convert input energy into contraction, enabling tasks like lifting or pulling weights [1, 2]. This input energy can come in various forms, such as physical or chemical factors [3, 4]. Artificial muscles can be any device or material that contracts in response to stimuli such as heat, electric current, pressure, temperature, or light [5]. These muscles have numerous applications, including wearable and rehabilitative devices, innovative surgical tools, biomimetic robots for search, rescue, and exploration, as well as components of robots like grippers, arms, and legs [6]. Their ability to perform contraction, expansion, and rotational movements makes them versatile in various systems.

Pneumatic artificial muscles (PAMs) are one of the oldest and most widely used artificial muscle types. These artificial muscles are characterized by a soft bladder that contracts in length upon inflation. PAM was first invented in the 1950s by atomic physicist Joseph L. McKibben for artificial limbs of the handicapped [7]. The most common and studied PAM is the McKibben muscle, featuring a cylindrical inner bladder and an external braid [8]. During inflation, the bladder expands radially, increasing the angle between braid strands and the long axis, resulting in actuator shortening [9]. In the 1980s,

the Bridgestone Company introduced a redesigned, more powerful PAM for industrial painting applications and those assisting disabled individuals and service robotics [10]. PAMs have also been utilized in biomedical applications such as the Human Muscle Enhancer (HME) system [11] and advanced robots such as walking/running machines and humanoid robots [12, 13]. PAMs offer significant advantages, such as being affordable, lightweight, soft, and safe for human interaction [14]. However, using these systems comes with notable challenges. PAMs can only function with positive pressure, as they collapse under vacuum conditions. Additionally, one of the main limitations of PAMs is their reduced portability due to the often-large space required for the fluid tank [5] and possible leakage [15].

Alternative types of artificial muscles can be employed to address the challenges faced by pneumatic muscles [16]. These new muscles utilize the shape memory effect (SME) of materials, converting energy into contraction or expansion. The concept of the shape memory effect is inspired by nature, as observed in carnivorous plants like *Drosera capensis*. When insects get trapped on their sticky surfaces, the leaves gradually fold around them to facilitate the insects' digestion process [17]. The SME in certain materials refers to their capacity to restore a deformation upon exposure to specific stimuli, such as temperature, electricity, magnetic fields, moisture, UV light, or other sources [18, 19]. These unique materials, known as shape-memory materials, belong to the category of smart materials due to their ability to adapt and respond to various stimuli [20].

Shape Memory Alloys (SMAs) are one of the materials that can be employed in shape memory-based artificial muscles [21]. SMAs primarily consist of two phases: Austenite and Martensite [22]. The transformation between these two phases in SMAs can enable contraction and expansion in artificial muscles. These materials offer benefits like a high force for movement, portability, and energy density for powerful actions [23]. However, they have drawbacks such as high density, mass, and limited stretching capacity, with a 6% contraction in SMA wire length. This restricts the achievable displacement through straightforward connections [24].

Shape Memory Polymers (SMPs) are another class of shape memory materials suitable for shape memory-based artificial muscles [25]. Compared to other shape memory materials, SMPs and their composites possess advantages such as lightweight, low cost, high elasticity, better strain recovery, lower programming temperature, improved processability, diverse material options, biocompatibility, and biodegradability [26–29]. Additionally, polymeric artificial muscles showcase superior responsiveness to multiple stimuli. SMPs can expand and contract more significantly than SMAs, making them appealing for applications requiring higher strain levels [30].

In recent years, with the advancement of additive manufacturing, or 3D printing, as an advanced production method and its integration with the shape memory effect, the novel field of 4D printing has emerged [31–34]. This innovative area has significant potential in the manufacturing of artificial muscles. 4D printing introduces a new dimension of time to 3D printing and enables the creation of intricate and customized structures for SMPs [35–37]. Consequently, this advancement has led to the production of improved actuators. However, there are no reported cases of 4D-printed artificial muscles in the literature. Nevertheless, there are many examples of using 4D printing to create soft actuators [38, 39]. Lalegani Dezaki and Bodaghi [40] developed a novel conceptual design of meta-laminar jamming (MLJ) actuators using a polyurethane shape memory polymer (SMP)-based meta-structure fabricated through 4D printing. They evaluated the mechanical properties of various SMP meta-structures and investigated shape memory effects and shape recovery. MLJ actuators with auxetic meta-structure cores showed better performance. These actuators can shape recover and lock without input power, lift and hold objects, and have potential applications as end-effectors and gripper devices [41, 42].

There are numerous constraints when utilizing 4D-printed rigid polymers for artificial muscles and actuators [43]. Initially, these rigid components are unsuitable for numerous applications that require safety, flexibility, and interaction with humans [44–46]. For instance, traditional robots often depict machines with rigid bodies and movements. Soft robotics, a new branch, aims to replace hard and inflexible components with soft and flexible materials to imitate life's actuation mechanisms [47, 48]. Conversely, the strain produced by rigid SMPs is relatively low and can obstruct the functional working distance of artificial muscles. As a result, in recent years, researchers have focused on developing soft artificial muscles with greater stretchability to expand the scope of artificial muscle applications. Roach et al. [49] developed a method to manufacture elastomeric artificial muscles using liquid crystal elastomer (LCE) fibers. They employed direct ink writing (DIW), creating a two-stage thermal-photo curing reaction between a difunctional acrylate monomer and thiol. By adding nano clay to increase viscosity, they extruded the LCE ink onto a rotating mandrel, obtaining long fibers. Post-printing, the fiber was first thermally cured on the mandrel, then mechanically stretched, and photocured for proper alignment, leading to stress-free reversible activation. Optimizing ink viscosity and DIW parameters resulted in fibers with impressive properties like 1.5 m length, 2 MPa modulus, 51% actuation strain, and over 100% failure strain used in artificial muscle. In another study, Duduta et al. [6] developed a soft composite dielectric elastomer actuator (DEA) made of strain-stiffening elastomers and carbon nanotube electrodes, achieving a peak energy density of 19.8 J/kg, close to the upper limit for natural muscles. This high-performance electrically driven soft artificial muscle can be applied in various fields, such as prosthetics, surgical robots, wearable devices, and soft robots for manipulation and locomotion in natural or human-centric environments. In our previous study [50], a direct pellet printing technique was developed for creating stretchable propylene-based elastomers. The filament buckling issues were overcome, and precise control over material flow was achieved, resulting in a uniform microstructure. That method was utilized to create a stretchable elastomer with exceptional elongation (4000%).

The current research focuses on developing highly flexible, soft elastomers with shape memory properties and 4D printability, aimed at addressing limitations in existing artificial muscle technologies. By utilizing a propylene-based elastomer as a soft, stretchable artificial muscle, this study achieves significantly higher actuation strains than other artificial muscles, enabling

efficient manipulation and lifting of various objects. The innovative design employs a simple dog bone geometry inspired by the chameleon's tongue, enhancing stretchability without complex geometries. Additionally, the incorporation of carbon black creates a nanocomposite elastomer, significantly improving mechanical properties during cyclic shape memory processes. This study highlights several novel aspects that distinguish it from previous work. This study is the first to report the development of 4D-printed artificial muscle. In addition, the stretchability of this artificial muscle is approximately 4000%, which far surpasses the stretchability of previously reported artificial muscles. The actuation strain in the presented artificial muscle is 148%, significantly higher than the typical 40%–50% strain found in McKibben-type PAMs. Another novel aspect of this study is the novel 3D printing method, direct pellet printing, which does not require filament and addresses the issue of filament buckling. The effect of carbon black addition on cyclic actuation and its impact on maintaining mechanical properties over multiple actuation cycles of artificial muscles has been investigated. The results demonstrate the potential of these 4D-printed elastomers to revolutionize artificial muscle applications in soft robotics and wearable devices.

2 | Materials and Methods

2.1 | Material

In this study, Vistamaxx 6202, a propylene-based thermoplastic elastomer (ExxonMobil, USA) pellets served as the primary raw material for direct pellet 3D printing of artificial muscle. In order to prepare elastomer nanocomposites, this study utilized carbon black nanoparticles (stock #: US1067) produced by US Research Nanomaterials Inc. (Houston, TX 77084, USA). The material properties are presented in Table 1.

TABLE 1 | Specifications of Vistamaxx pellets and carbon black as feedstock materials.

Specifications of Vistamaxx pellets	
Appearance/form	Transparent/ Pellets
Density (g/cm^3)	0.862
Hardness (shore A)	64
Ethylene content (%)	15
Melt Flow Index (g/10 min)	9.1
Melt-Mass-Flow Rate (MFR) (g/10 min)	20
Specifications of carbon black	
Purity	> 95%
Thickness	30–150 nm
Diameter	200–800 nm
PH	9.8
True Density	0.38 g/mL
H_2O	< 5%
Ash	< 3.2%
Specific Surface Area	> 700 m^2/g

2.2 | Processing of Elastomer-CB Nanocomposites

By combining polymers with different fillers, we can create polymer composites that have improved properties [51]. Carbon black nanoparticles are a type of low-cost, conductive material that can be effectively combined with elastomers to improve their electrical conductivity, mechanical strength, and physical properties. Munir et al. [52] have used composites of bio-based polyurethane filled with carbon black nanoparticles to create a conducting polymer.

In this study, elastomer-CB nanocomposites were prepared using a melt mixing technique with a Brabender internal mixer (Brabender, Germany). The process involved three varying concentrations of CB nanoparticles: 1%, 2%, and 4%. Initially, Vistamaxx 6202 granules were melted within the mixer at 190°C and a speed of 60 rpm for 2 min. Subsequently, CB nanoparticles were incorporated into the melt. The mixer continued to operate for an additional 8 min to ensure uniform distribution of nanoparticles within the elastomer matrix. The resulting material was obtained in a lump form, which was then processed using a press machine. A hot press at 190°C and a cold press with 60 kPa pressure were employed to transform the lumps into 1 mm thick sheets. These sheets were subsequently cut into granules, suitable for direct pellet printing. Figure S1 (Data S1) illustrates the preparation process of nanocomposite pellets prior to the commencement of the printing process.

2.3 | Direct Pellet Printing

In this study, we employed the same direct pellet printer from our previous research [50, 53] to print soft elastomeric pellets. This approach helps overcome the common issue of filament buckling when printing soft materials using conventional filament-based extrusion in Additive Manufacturing [54, 55]. A syringe-based feeding mechanism was utilized, consisting of a cylinder and a piston. The raw material was loaded within the heated cylinder, and the piston, driven by gas pressure (pneumatic pressure), applied pressure on the molten material. This facilitated its flow through the nozzle and deposition onto a bed, similar to the Fused Deposition Modeling (FDM) process. Adjustable air pressure allows for controlling the material flow effectively. The printing parameters used for sample production in this study are detailed in Table 2.

2.4 | Tensile Characterization

In this study, the mechanical characteristics of a 3D-printed elastomer and its composites were investigated using a Santam machine with a load cell capacity of 100 kg at room temperature. To maintain consistency, the tensile test samples were 3D printed according to the ASTM D638 type V standard, and the printing parameters outlined in Table 2 were utilized. The specimens were subjected to uniaxial tension testing at a strain

TABLE 2 | Printing parameters.

Extruder temperature	Nozzle diameter	Print speed	Layer height	Infill density	Pneumatic pressure	Printing time	Raster angle
205°C	0.6 mm	200 mm/min	0.4 mm	100%	2 bar	28 min	0° and 90°

rate of 100 mm/min until failure. To guarantee accurate results, the tests were conducted in triplicate, and the findings were expressed as the mean (M) value. In addition, we excluded outlier data points that varied significantly from the rest of the dataset. The dimensions of the printed samples, based on ASTM D638 standards, as well as the actual printed samples, are depicted in Figures S2 (Data S1).

2.5 | Scanning Electron Microscopy

A VEGA Scanning Electron Microscope (produced by Tescan Company) was employed according to the ASTM (F1877-05) standard to examine the morphology, distribution of nanoparticles, and their compatibility with the elastomeric matrix. Furthermore, the investigation included assessing layer adhesion and potential printing defects in 3D printed parts to evaluate their print quality and printability. The SEM has a magnification range of 20× to 100,000×, a voltage range of 5 to 30 kV, and a vacuum level of 10^{-5} Pa. To prepare the samples for imaging, the freeze fracturing method was conducted using liquid nitrogen. Before the imaging process, the freeze-fractured samples were coated with gold to improve their conductivity.

2.6 | Cyclic Shape Memory Effect

In this study, the shape memory process of printed elastomers involves three primary stages. Initially, the samples of length L_0 undergo strain at room temperature (cold programming) and attain length L_1. It is notable that the role of programming temperature is important in shape memory polymers, where entanglements act as net points for shape memory in them. This effect has been studied by Soleyman et al. [56]. Subsequently, upon unloading, the elastic component recovers a portion of the deformation due to the elastic nature of the elastomer. However, the plastic deformation remains in the samples, representing a temporary shape with length L_2. Finally, when exposed to heat, the samples can revert to their original shape prior to loading.

A crucial aspect of artificial muscles is their ability to maintain functionality and mechanical properties throughout their working cycles. In this study, the shape memory process was repeated for 5 cycles to evaluate the mechanical properties after each cycle. To accomplish this, tensile samples were stretched to a specific strain level, and a stress–strain curve was plotted during this process. It is worth mentioning that to assess the impact of strain level, two sets of samples were tested using two distinct strain levels (750% and 1400%). Once the desired strain was reached, the load was removed, and the elastic deformation recovered immediately. The samples were then immersed in 70°C water to regain their original shape. The recovered sample underwent another tensile test, and the cycle was repeated. This cyclic shape memory test is illustrated schematically in Figure S3 (Data S1).

2.7 | Soft Stretchable Artificial Muscle

In the previous section, it was explained that after unloading, samples recover their elastic deformation while retaining

plastic deformation, forming a temporary shape. This temporary shape can function as a soft, stretchable artificial muscle capable of contracting and lifting objects. To achieve this, cold programming of the samples was performed at room temperature, allowing them to undergo elastic recovery and adopt a temporary shape. These pre-strained samples were then utilized as "muscles" to lift objects by fixing them on one side and attaching the object to the other side. Two heat guns were employed to heat the sample, causing it to recover its original shape and lift the object. During the shape recovery of the artificial muscle, two heat guns blow hot air from both sides of the sample to ensure uniform heating. In addition, the temperature remained constant for both heat guns during the test. The heat distribution is uniform in the samples due to their small thickness. The experimental setup is illustrated in Figure 1.

In this study, the printed elastomer and its nanocomposites were utilized to lift a light object, a table tennis ball (3 g), and a heavier object, a racket (95 g). During the lifting process, the lifting distance was measured, and a time-distance plot was drawn. Additionally, the work done by the muscles was calculated using the Equation (1).

$$W = F \times \Delta H \tag{1}$$

In which W denotes the work accomplished by the muscle, F signifies the force exerted and lifted, and ΔH represents the distance through which the object is elevated by the muscle's action.

The geometry of artificial muscles is intricate and challenging to manufacture in various instances [57]. For instance, in artificial muscles made from polymers, the materials are often designed in specific forms, such as twisted coils or special structures [58–60]. In this study, we employed a simple design similar to the geometry of tensile test specimens for artificial muscles. This concept and geometry were inspired by one of nature's most elastic muscles, the chameleon's tongue muscle [61]. Chameleons use a unique ballistic tongue projection mechanism among lizards to capture prey. Their tongue can extend up to two full body lengths and reach 600% of its resting length during hunting [62]. Disregarding the ballistic mechanism, the geometry of the chameleon's tongue muscle is advantageous for stretching and retracting while hunting insects. As depicted in Figure 2a, the chameleon's tongue muscle is anchored on one side, with the folded muscle starting wider than the tongue's middle. At the tongue's tip, there is a sticky pad that the chameleon uses to catch its prey [63]. The beginning of the muscle, which is folded, aids in the tongue's enhanced stretching and retracting capabilities during the catching process. The slimmer middle portion of the tongue facilitates stretching, while the sticky tip is responsible for gripping objects. This mechanism resembles the ultra-stretching feature observed in our samples, as depicted in Figure 2b. One of the clamping areas in the sample contributes to sticking to objects. The reduced section is responsible for stretching and recovering. Another fixed clamping area assists in stretching the reduced section further by providing Data S1 during extension and recovery, as illustrated in Figure 2c.

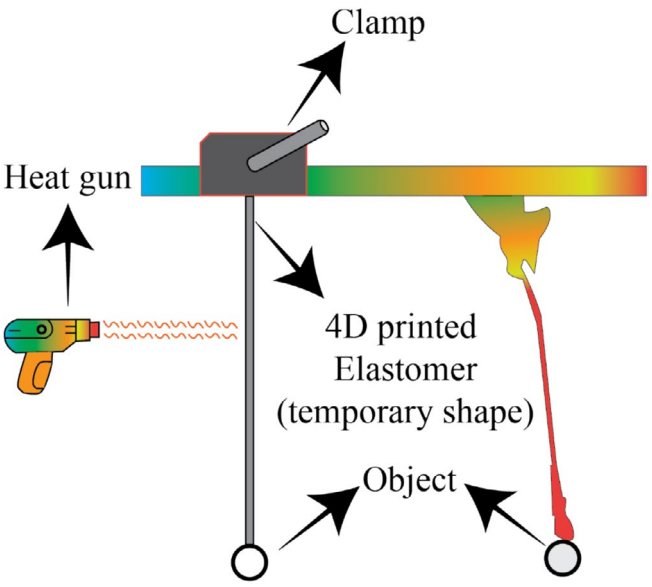

FIGURE 1 | The experimental setup for lifting objects by 4D-printed elastomeric artificial muscle. [Color figure can be viewed at wileyonlinelibrary.com]

3 | Results and Discussion

3.1 | Tensile Characterization

In Figure 3, stress–strain curves from the tensile test of the printed elastomer and its nanocomposites with different carbon black content are displayed until their breaking point. As mentioned previously, tensile tests were repeated three times for each sample. The actual experimental results for elongation at break and UTS are presented in Table S1 (Data S1). The printed elastomer without CB incorporation exhibits high stretchability and soft nature, characteristic of elastomeric materials. This sample has an elongation at break of approximately 4048%, which can be beneficial for applications requiring high stretchability such as stretchable electronics and soft robotics. The mechanism of high stretchability of this material has been discussed in our previous study [50]. The ultimate tensile stress (UTS) for this sample is 3.71 MPa, which might limit its use in highly stressed applications. In samples containing carbon black nanocomposites, the material demonstrates a stiffer behavior. As depicted in Figure 3, the nanocomposites exhibit a steeper slope in the elastic region, indicating a higher Young's modulus. Additionally, these samples typically experience higher stresses compared to pure elastomer at the same strain. This can be attributed to the reinforcing effect of nanocomposites [64]. Conversely, with carbon black addition, the stretchability of the samples decreases. This can be attributed to the interaction between nanoparticles and the polymer matrix, where dispersed nanoparticles can obstruct the movement of polymer chains, leading to a reduction in polymer elongation [65]. Designers, based on the application, can choose between elastomer nanocomposites that can withstand more stresses with lower elongation at break or pure elastomers to enhance stretchability.

In nanocomposite samples, which generally exhibit similar behavior, the sample with 1% carbon black showed the poorest mechanical properties, featuring 2392% elongation at break and

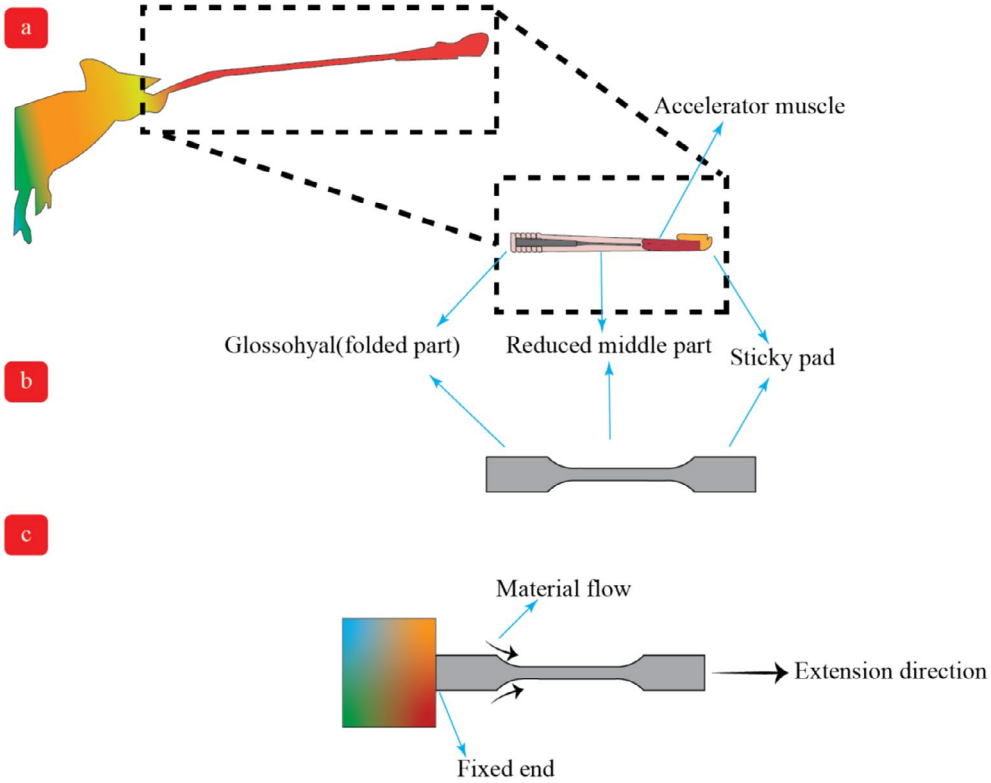

FIGURE 2 | Bio-inspired design of: (a) Chameleon's tongue parts, (b) Similar parts on artificial muscle, and (c) Mechanism of providing Data S1 during extension. [Color figure can be viewed at wileyonlinelibrary.com]

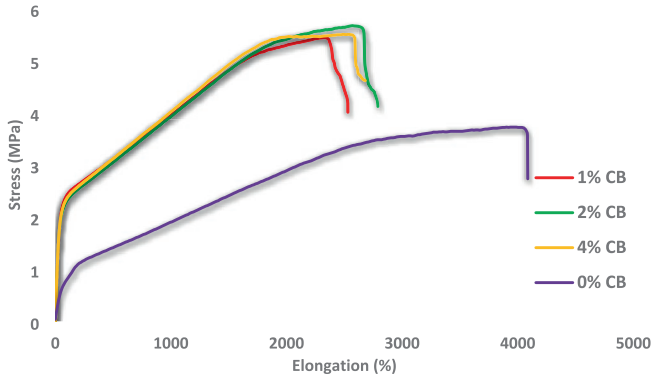

FIGURE 3 | Stress–strain curves of printed elastomer and its nanocomposites. [Color figure can be viewed at wileyonlinelibrary.com]

5.47 MPa UTS. The best mechanical properties are observed in the sample with 2% CB, 2665% elongation, and 5.58 MPa UTS. This improvement in mechanical properties with higher CB content is supported by previous research [66]. However, the sample with 4% CB displayed weaker mechanical properties than the 2% CB sample, with 2583% elongation at break and 5.47 MPa UTS. This can be attributed to the increased likelihood of agglomeration at higher CB amounts, causing nanoparticles to cluster together and form potential sites for crack initiation [67]. This phenomenon can be visually observed in the morphological investigations presented in the next section.

The mechanical properties of the elastomer samples, including UTS and elongation at break, were statistically analyzed using one-way analysis of variance (ANOVA). Detailed ANOVA results are provided in the supplementary file for further reference. Tukey's Honestly Significant Difference (HSD) test was used to identify which specific group means differ significantly after an ANOVA indicates overall significance. Tukey's HSD results for elongation at break and UTS are presented in Tables S2 and S3 (Data S1), respectively. The results of ANOVA and Tukey's HSD test suggest that the addition of CB significantly influences the mechanical properties of the elastomer. The 2% CB sample demonstrated a balance between UTS and elongation at break, making it a promising candidate for applications requiring both strength and flexibility. This sample's elongation at break is significantly better than the 1% CB and 4% CB samples, although no significant difference was observed in their UTS. The mean UTS of the 2% CB sample is higher than that of the 1% CB and 4% CB samples, as shown in Figure S4 (Data S1).

3.2 | Scanning Electron Microscopy

In material extrusion additive manufacturing, which involves extruding material through a nozzle and depositing it onto a substrate, the nozzle's geometry determines the shape of the extruded material. Typically, the nozzle has a circular hole for material extrusion, resulting in cylindrical beads. These beads are stacked to create 3D objects. As illustrated in Figure 4, the cylindrical nature of the beads leaves gaps between layers and beads in the printed samples, which reduces the mechanical properties of the printed object compared to molded ones [68]. This is due to the gaps being susceptible to crack initiation during material loading. These gaps, referred to as inter-voids in some resources [69], are indicators of the printing process's quality. The size of these gaps depends on

the print parameters and material printability, with better overlap, material flow, and wettability leading to smaller cavities between layers and beads, resulting in a more uniform microstructure and improved mechanical properties [70].

In this study, scanning electron microscopy (SEM) is employed to examine 3D printing quality, layer adhesion, and potential printing defects. To achieve this, SEM images with lower magnifications (50×) are captured from the cross-section of a freeze-fractured elastomer and its nanocomposite with varying CB compositions. The resulting images for 0%, 1%, 2%, and 4% CB are displayed in Figure 5a–d, respectively.

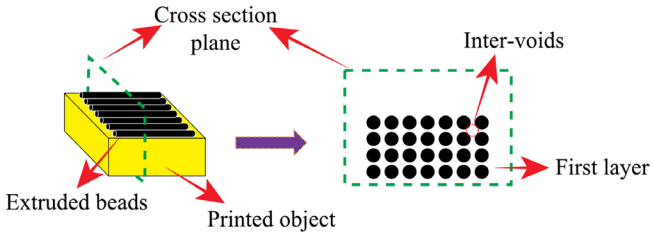

FIGURE 4 | Inter-voids between layers in the cross-section of a printed part. [Color figure can be viewed at wileyonlinelibrary.com]

In Figure 5, all samples exhibit a uniform microstructure with well-bonded layers and beads, demonstrating the importance of adjusted printing parameters and flow control for high-quality printed samples. These samples show no signs of delamination, lack of fusion, or fractures, leading to the desirable mechanical performance of printed samples. Inter-voids, a common feature in material extrusion processes, are present in all samples [71]. However, due to proper material flow, many voids are filled, and the remaining ones are small. Some of these voids are highlighted with yellow circles in Figure 5. As the CB content increases, the number and size of these voids also increase, and printing quality decreases. The printing parameters kept constant for all samples, play a crucial role in controlling void size. This decrease in printability is due to the fact that the addition of CB nanoparticles can alter the viscosity of the elastomer nanocomposite [72, 73] with higher concentrations, causing increased viscosity and making it more difficult for the material to flow and fill gaps compared to low-viscosity melts.

In this research, we employed high-magnification SEM images to analyze the distribution of nanoparticles within a polymer matrix. This factor significantly influences the material's mechanical and shape memory properties. The obtained images are displayed in Figure 6.

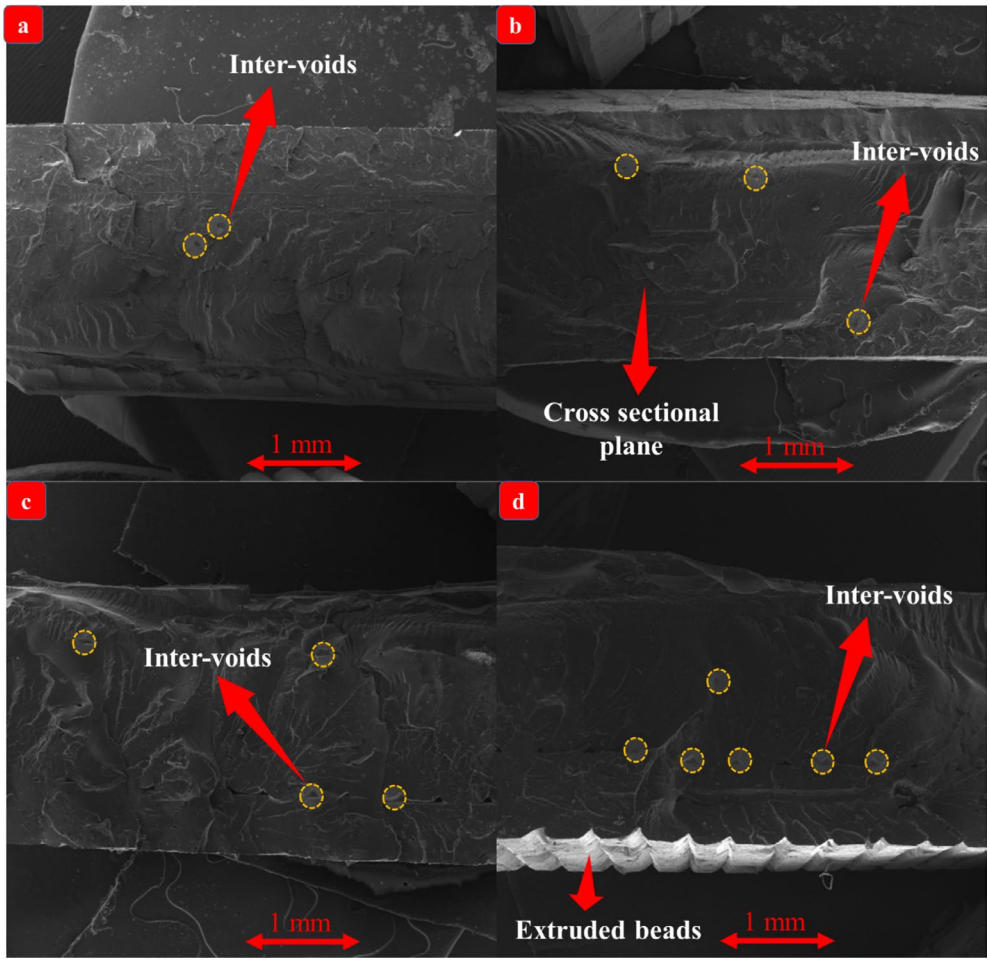

FIGURE 5 | Low magnification (50×) SEM images for investigating printing quality for elastomer nanocomposites with different CB content: (a) 0%, (b) 1%, (c) 2%, and (d) 4%. [Color figure can be viewed at wileyonlinelibrary.com]

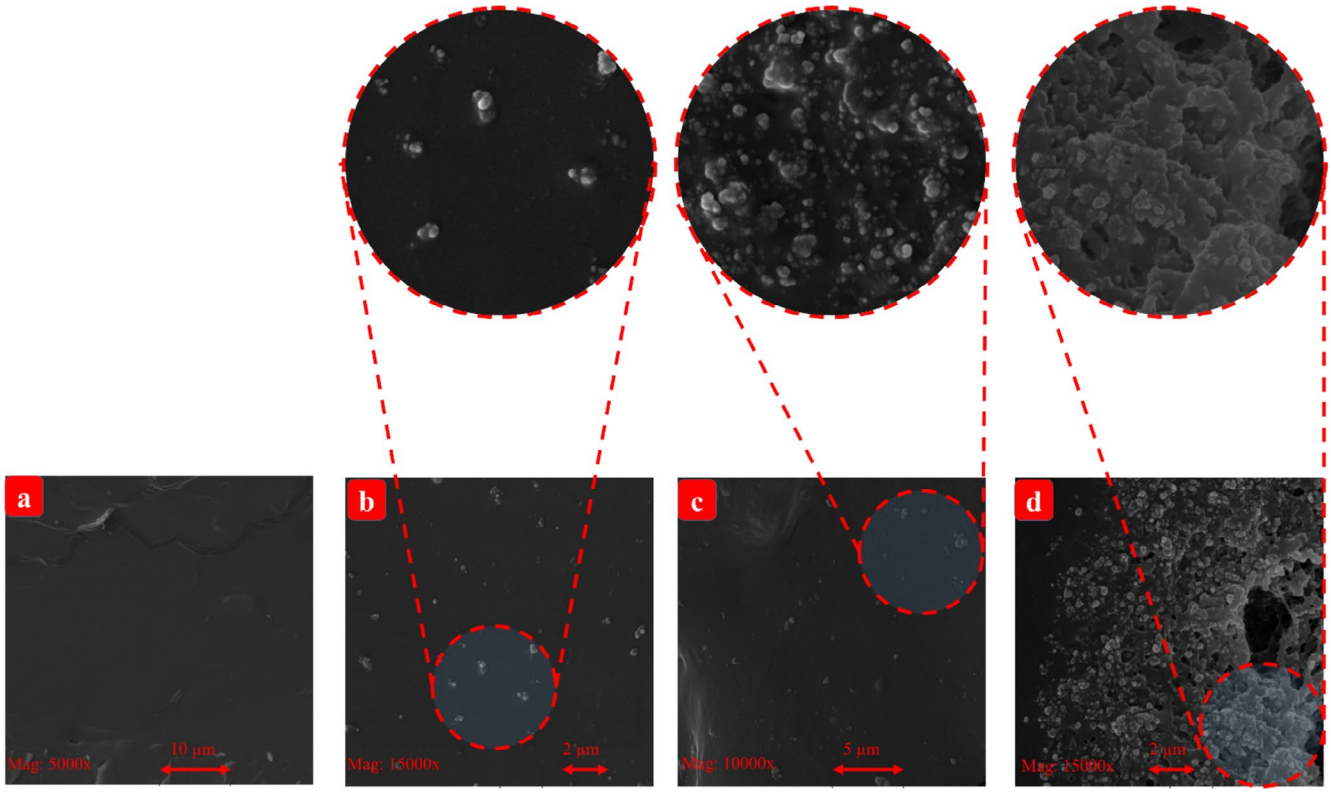

FIGURE 6 | High magnification SEM images (36,000× for zoomed SEMs) for investigating nanoparticle dispersion in elastomer nanocomposites with different CB content: (a) 0%, (b) 1%, (c) 2%, and (d) 4%. [Color figure can be viewed at wileyonlinelibrary.com]

In Figure 6, CB nanoparticles can be distinguished due to their brighter color in the dark polymer matrix. In Figure 6a, which represents a neat elastomer, there are no nanoparticles present in the sample.

CB nanoparticles have a natural tendency to cluster or agglomerate. As the concentration of CB nanoparticles increases, the likelihood of agglomeration also rises [74]. In the sample with 1% CB (Figure 6b), a desirable dispersion of nanoparticles without any agglomeration can be observed. The nanoparticles and the matrix have strong adhesion at their interface, with no breaks or separations at the boundary between the matrix and nanoparticles. If there were poor adhesion between the carbon black and elastomer, small holes would appear on the broken surface because of the separation of carbon black from the matrix. In Figure 6c, when the CB content increases to 2%, the number of nanoparticles in a specific area of the sample also increases. However, minor nanoparticle agglomeration can be found in the cross-section of printed samples, which does not significantly impact the sample's unity or cause any defects. As shown in Figure 6d, when the CB content reaches 4%, severe clustering of nanoparticles occurs in the sample, leading to hole formation and discontinuity. These agglomerations are responsible for the reduced mechanical properties of 4% samples compared to 2%. Guo et al. [75] studied the impact of CB agglomerations on the mechanical properties of a nanocomposite made of PLA and CB. In addition, the size distribution of CB in elastomer-CB nanocomposites was analyzed using ImageJ software to investigate the effect of CB concentration on dispersion. As shown in Figure S5 (Data S1), higher CB concentrations resulted in larger particle diameters due to increased agglomeration. However, the sample with 1% CB exhibited more uniform dispersion and smaller particle sizes, likely due to reduced intermolecular forces and cohesive interactions at lower concentrations.

3.3 | Shape Memory Behavior Mechanism and Theoretical Framework

Shape Memory Polymers (SMPs) consist of two primary components. The first part stores elastic energy without relaxation, maintaining the sample's permanent shape. The second part retains the stored energy and releases it upon temperature change, known as the switching phase. Energy barriers are involved in this switching process. For the polymer chains to store elastic deformation without significant relaxation, they must be connected. These connections are referred to as "net points." A switching phase is necessary to prevent the elastic strain from being recovered before the switching phase is removed [76]. Typically, this switching phase corresponds to the glass transition temperature. However, in our material's case, the glass-transition temperature is below zero, making the shape memory mechanism different.

Vistamaxx 6202, the elastomeric matrix used in this study and produced by ExxonMobil (USA), is a well-known propylene-based elastomer (PBE) with 85% isotactic propylene repeat units and a 15% random ethylene distribution. Metallocene catalyst technology is employed in its creation. This PBE has a unique microstructure, featuring physical cross-links between hard segments (PP) with high melting or glass transition temperatures (T_g) and soft segments (PE) with low T_g. This results in

a combination of elasticity found in traditional elastomers and recyclability from thermoplastics [77]. Under strain-induced deformation, soft segments stretch while hard parts act as anchoring points for elastic recovery. It is worth noting that in CB-filled polymers, CB enhances shape memory properties by promoting bound rubber formation. Bound rubber refers to polymer chains immobilized on the surface of CB particles. These immobilized layers act as anchors within the matrix, improving shape memory behavior through restricted chain mobility and enhanced interfacial interactions.

The shape memory effect in this thermoplastic elastomer is achieved through plastic deformation or cold programming. When strain is increased significantly, plastic deformation occurs in the sample, and the material cannot fully recover (relax). This can be due to polymer chain entanglements, which function as physical net points. In this situation, after elastic recovery at room temperature, the elastomer retains a temporary shape. This process, known as cold programming, is studied by Soleyman et al. [56]. After programming, heating the sample increases the free volume and entropy of the system. This allows the entanglements (physical net points) to release and return to their original shape.

This behavior can be explained using the generalized Maxwell model (Equation 2). The generalized Maxwell model is a widely used constitutive model for describing the viscoelastic behavior of polymers [78]. It explains the immediate and time-dependent recovery of a polymer when stretched by incorporating multiple Maxwell elements in parallel. The generalized Maxwell model consists of multiple Maxwell elements, each with a spring and dashpot in series, connected in parallel [79]. This allows the model to capture the multi-relaxation behavior observed in polymers.

$$\sigma(t) = \sum_{i=1}^{n} E_i \varepsilon_e^i(t) + E_\infty \varepsilon(t) \tag{2}$$

Where $\sigma(t)$ is the total stress, E_i are the spring moduli of the Maxwell elements, ε_e^i are the elastic strains in each Maxwell element, E_∞ is the modulus of the equilibrium spring, and $\varepsilon(t)$ is the total strain.

When a polymer is stretched and then released, it exhibits both immediate and time-dependent recovery. The portion of the strain recovered immediately upon unloading is attributed to the equilibrium spring in the generalized Maxwell model. This represents the instantaneous elastic response of the polymer. The remaining portion of the strain is recovered over time due to the relaxation of the Maxwell elements. As time passes, the stresses in the Maxwell elements relax, allowing the polymer to recover the remaining strain. The generalized Maxwell model captures this behavior by combining the instantaneous elastic response with the time-dependent relaxation of the Maxwell elements. The number of Maxwell elements and their respective moduli and relaxation times determine the specific shape of the recovery curve and the relative contributions of immediate and time-dependent recovery.

The recovery behavior of polymers depends on both time and temperature, which is similar to the classical Time–Temperature Superposition (TTS) principle observed in polymer materials. In polymer physics, the thermal motion of molecules causes the same relaxation processes to occur. This means that relaxation can happen over a longer period at a lower temperature or over a shorter period at a higher temperature [80]. The TTS principle can be used to understand the shape memory behavior of TPE samples used as artificial muscles. When a polymer sample is stretched and released, it recovers a portion of the strain immediately. The remaining portion of the strain is recovered over time. By applying higher temperatures, the time-dependent recovery portion can be accelerated. This is because higher temperatures increase the mobility of the polymer chains, allowing them to relax and recover the strain more quickly. In other words, the same amount of time-dependent recovery that would normally take a long time at a lower temperature can be achieved much faster by increasing the temperature.

According to the TTS principle, changing the temperature can be viewed as shifting time along the logarithmic horizontal axis. If we define a new horizontal axis called the reduced annealing time t_r after applying the TTS principle, it can be expressed as Equation (3) [81]:

$$t_r = \frac{t}{a_T} \tag{3}$$

Where the shift factor a_T, which indicates how much the time axis shifts at different temperatures, can be calculated using the Williams–Landel–Ferry (WLF) equation (Equation 4).

$$\log(a_T) = -\frac{C_1[T - T_{ref}]}{C_2 + T - T_{ref}} \tag{4}$$

Where T_{ref} is the reference temperature and C_1 and C_2 are materials constant. Based on the WLF equation, as temperature increases, the time required for a polymer to relax decreases.

The discussed shape memory process of TPEs offers both benefits and drawbacks. A notable advantage is its ability to be programmed at room temperature through strain without heating and cooling, a common practice for other SMPs with glass transition temperature (T_g) switching phases. The material's rubbery nature facilitates high-strain recovery and stretchability in various applications. However, this process has limitations, such as high immediate relaxation or elastic recovery in TPEs, which results in low shape fixity.

3.4 | Cyclic Shape Memory Test

To evaluate the changes in the mechanical properties of samples following multiple shape memory processes, a shape memory cyclic test was conducted, and the results are displayed in Figure 7. The left column represents test results with a strain level of 750% for the tensile test, while the right column has 1400%. Each curve in the figure is labeled with a combination of CB percentage and cycle number. For instance, 1% CB C4 refers to a sample with 1% CB concentration and the fourth cycle of the cyclic shape memory test. It is worth mentioning that the initial sample, as-printed, exhibits the best mechanical properties.

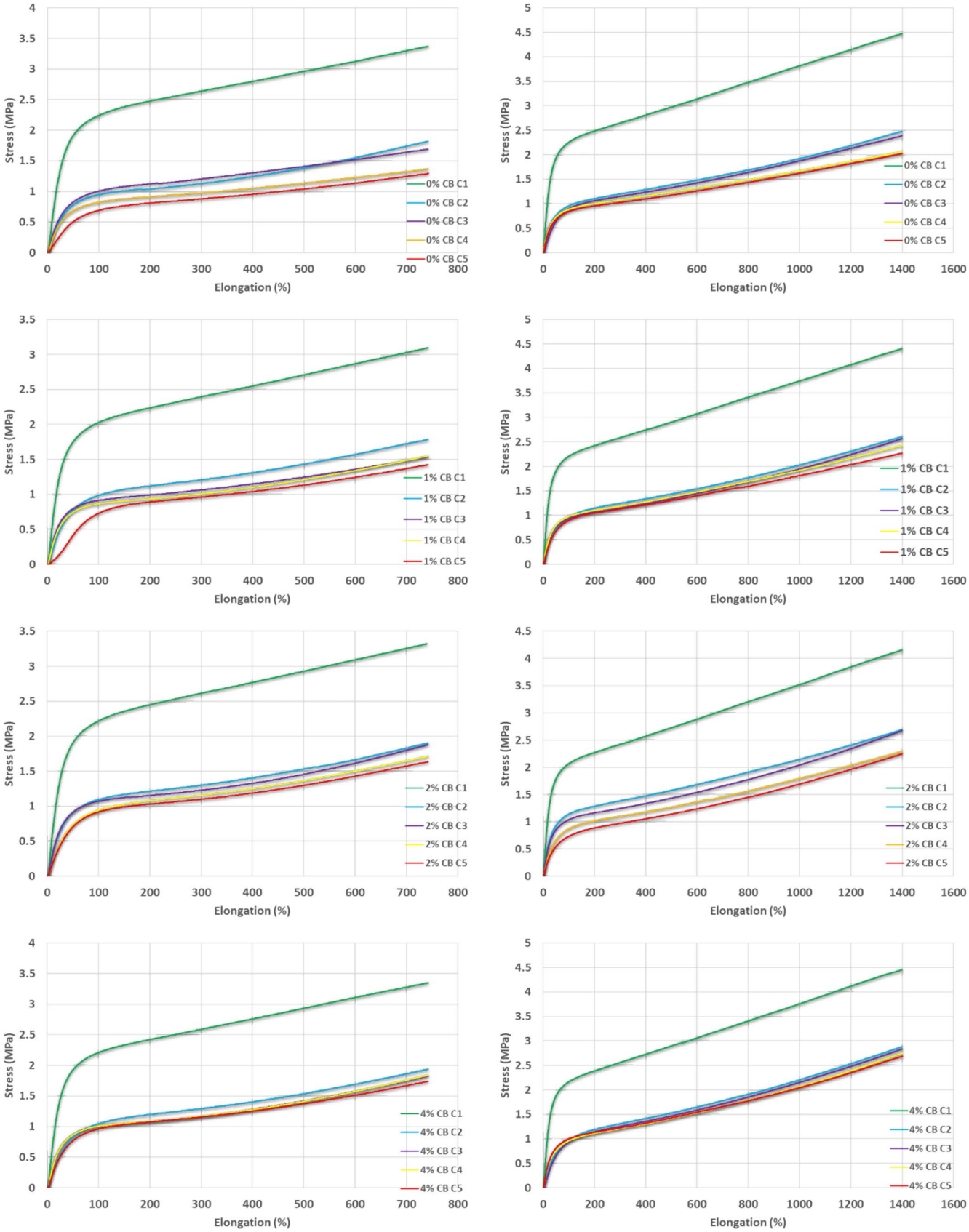

FIGURE 7 | Cyclic shape memory test results for samples with different CB concentrations and different strain levels: Left column test results with a strain level of 750% and right column test results with a strain level of 1500%. [Color figure can be viewed at wileyonlinelibrary.com]

However, a significant drop in mechanical properties can be observed after the first cycle of shape memory. Following that, the mechanical properties decline at a less significant rate, and the samples approach a steady state of mechanical properties. This trend is consistent across all samples, as each cycle demonstrates lower mechanical properties than the previous one. This implies that with each shape memory process, which involves straining and heating, the recovered sample's mechanical properties are inferior to the original sample.

The observed changes in mechanical properties of samples during shape memory cycles can be attributed to three primary factors: high strain levels, the cumulative effect of stress and strain, and the heating process for shape recovery. The samples undergo high strain levels (750% or 1400%), which may cause damage to the material, particularly weak polymer chains. These damaged chains may not contribute to load-bearing in subsequent cycles. Another factor that could contribute to the changes in mechanical properties during shape memory cycles is the cumulative effect of stress and strain experienced by the samples. As the samples undergo multiple shape memory processes, they may develop microscopic cracks or structural alterations due to the repetitive loading and unloading. These changes can affect the overall mechanical properties of the samples, causing them to deviate from their original state. The heating process for shape recovery can also contribute to reduced mechanical properties. The mechanical properties of polymers are highly dependent on their thermomechanical history. In the first shape memory cycle, most weak polymer chains are torn, resulting in a significant drop in mechanical properties. After that, there are fewer weak chains to be torn, leading to less significant drops in mechanical properties. Eventually, after tearing all the weak areas in the polymer structure, the mechanical properties reach a steady state.

To analyze the impact of strain levels on mechanical properties, one can compare the data presented in the left and right columns of Figure 7. It is observed that samples with a 1400% programming strain exhibit a slight decrease in strength after five cycles compared to those with a 750% strain. To quantify this difference, Equation (5) can be used to calculate the percentage drop in strength after five cycles:

$$\frac{\text{As printed strength in 750\% strain} - \text{5th cycle strength in 750\% strain}}{\text{As printed strength in 750\% strain}} \times 100 \quad (5)$$

The calculated percentage change in mechanical properties after completing five cycles of shape memory at 750% strain is provided in Table 3. In the provided table, it is noticeable that the decrease in strength following a cyclic shape memory test is more significant for a programming strain of 1400%. This can be attributed to the increased likelihood of separation in weak polymer chains and intermolecular bond disruption at higher strains.

Furthermore, Table 3 demonstrates the impact of carbon black addition on the data. As observed in the table, as the CB content increases, the decline in mechanical properties lessens. This is due to the reinforcement effect of CB in the elastomeric matrix. In addition, the immobilized polymer molecules by CB (bound rubbers as discussed previously) mitigate mechanical property degradation during repeated actuation cycles by reducing chain slippage. This result can also be visually observed in Figure 7. The incorporation of carbon black enables shape memory elastomers to achieve a steady state more quickly and at higher stress levels with lower drops. In applications requiring stable mechanical properties of shape memory elastomers, CB can be an effective addition to prevent a drop in mechanical properties.

TABLE 3 | Percentage drop in strength after completing five cycles of shape memory in 750% strain.

	Programming strain level	
	750%	**1400%**
0% CB	60%	60%
1% CB	54%	54%
2% CB	50%	53%
4% CB	48%	49%

3.5 | Soft Stretchable Artificial Muscle

About the shape memory effect of 4D printed elastomers, an investigation into using them as artificial muscles, inspired by the chameleon's tongue, was conducted.

A table tennis ball is lifted using a 4D-printed neat elastomer and its nanocomposite. This application of 4D-printed artificial muscle can be used in lifting miniature objects. Videos S1 and S2 showcase these demonstrations. The lifting process for the neat elastomer and its composite is displayed in Figure 8a,b, respectively, through multiple frames.

The calculation of work performed on the depicted sample in Figure 8a,b can be executed as follows:

$$W_a = mg\Delta H = 3 \times 10^{-3} \times 10 \times 10^{-2} = 0.3mJ \quad (6)$$

$$W_b = mg\Delta H = 3 \times 10^{-3} \times 6 \times 10^{-2} = 0.18mJ \quad (7)$$

In Figure 8, the artificial muscle printed with pure elastomer can achieve strain up to 148% (10 cm) from a temporary to a permanent shape, while one printed with elastomer nanocomposite achieves 86% strain (6 cm). This difference occurs because the pure elastomer can elongate more than its composite counterparts. However, incorporating carbon black in the elastomer allows shape memory elastomers to reach a steady state faster and at higher stress levels, with minimal decline in mechanical properties. Conversely, typical McKibben-type PAMs are limited to approximately 40%–50% strain under no load [9]. Table 4 shows a comparison between the artificial muscle presented in this study and other artificial muscles and actuators.

Figure 9 displays a graph illustrating the relationship between contraction and time for the artificial muscle printed of pure elastomer. Initially, the shape recovery rate is fast; however, as the process continues, the contraction rate gradually decreases.

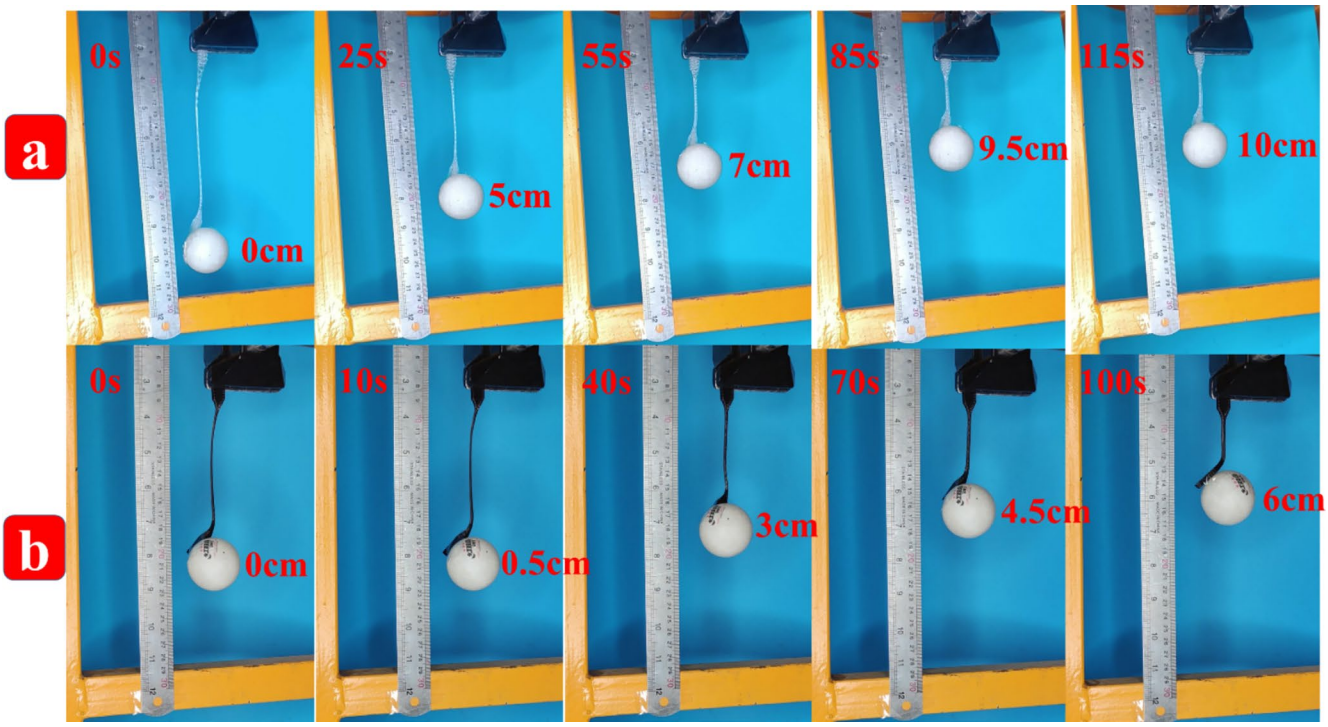

FIGURE 8 | The lifting process of 4D-printed: (a) neat elastomer and (b) elastomer nanocomposite. [Color figure can be viewed at wileyonlinelibrary.com]

TABLE 4 | Comparison between the 4D-printed artificial muscle and other artificial muscles and actuators.

Number	Type/Material	Actuation/ Contraction strain	Response time/rate	Other explanations	Energy source	Ref.
1	Polyolefin elastomer/ Biomass lignin	41%	—	< 700% EL	Thermal and electrical	[82]
2	LCE	80%	0.4 mm/s	Accordion-like deformation	Light	[83]
3	Liquid metal elastomer	87%	15 mm/s	Low driving voltage	Electrical	[84]
4	Twisted coiled actuator	48%	30 mm/s	—	Preloading of the fibers	[85]
5	Magnetic nanoparticles/ coiled muscles	30.6%	—	1.3 N force	Radio frequency magnetic field	[86]
6	PAM	35.8%	—	Novel winding method	Pneumatic	[87]
7	PAM	23.84%	0.0318 s	Rapid response	Pneumatic	[88]
8	DEA	50.6%	—	Self-healable	Electrical	[89]
9	LCE	60%	< 0.2 s	Microfiber actuator	Thermal	[90]
10	TPE/CB	148%	1 mm/s	> 2000% EL	Thermal	This work

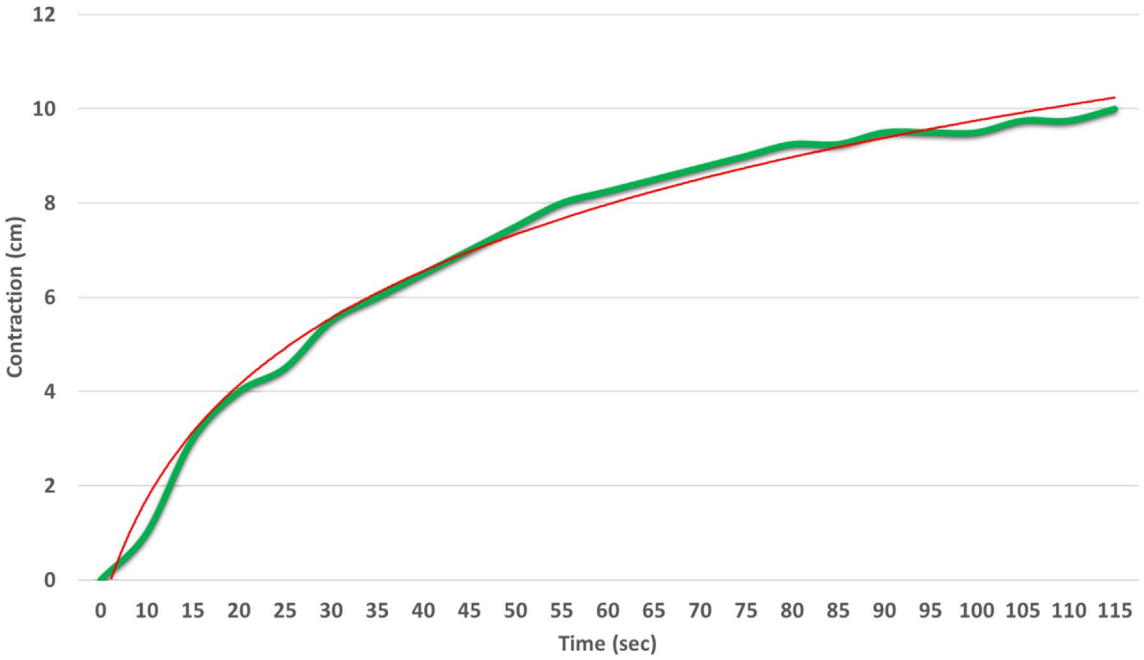

FIGURE 9 | Relationship between contraction and time for the artificial muscle printed of pure elastomer. [Color figure can be viewed at wileyonlinelibrary.com]

A logarithmic curve can be used to represent the given data quite well, as indicated by the high R-squared value of 0.9892. The equation for this curve is:

$$y = 3.4849ln(x) - 0.6889 \quad (8)$$

This plot demonstrates that a logarithmic curve can effectively express the dynamic behavior of the printed muscle. This indicates that, in the initial stages of heating, the contraction speed is high due to the rapid activation of the switching phase. During this stage, a 5 cm contraction occurs in just 30 s, resulting in a response rate of 1.7 mm/s. Subsequently, activation of the remaining switching phases requires more energy and, consequently, takes longer. The average response rate of the muscle is 1 mm/s. While this is slower than that of PAMs, larger contractions are more essential than a fast response in some applications.

Video S3 demonstrates the capability of a 4D-printed artificial muscle to lift heavier objects. In this demonstration, the artificial muscle lifts a table tennis racket. As the load increases, the strain that the artificial muscle can handle decreases.

4 | Conclusion

This research developed a new soft artificial muscle using 4D printing technology, utilizing highly stretchable thermoplastic elastomer (Vistamaxx) and its carbon black nanocomposites. A direct pellet printing technique was employed to overcome common issues with filament-based 3D printing. Mechanical properties were assessed using uniaxial tensile testing, and morphology was examined via scanning electron microscopy. Print quality and layer adhesion were also evaluated. Shape memory properties were tested through cyclic deformation and recovery, demonstrating the material's ability to recover its original shape while retaining some plastic deformation. The temporary shape functioned as a soft, stretchable artificial muscle capable of contracting and lifting objects. The printed material successfully lifted a light table tennis ball and a heavier racket, with measurements of distance, time, and work done. Inspired by the chameleon's tongue muscle, the design is simple, resembling tensile test specimens, yet highly effective. The main results indicate that 4D-printed elastomers have significant potential for applications in soft robotics and other fields requiring high elasticity and mechanical performance. The printed elastomer without CB exhibits exceptional stretchability, with an elongation at break of approximately 4048%. However, its UTS of 3.71 MPa may limit its use in highly stressed applications. The addition of carbon black nanoparticles to the elastomer improves its mechanical properties, including higher Young's modulus and UTS, but decreases its stretchability. The optimal balance of mechanical properties is achieved in the sample with 2% CB, which has an elongation at break of 2665% and UTS of 5.58 MPa. Higher CB content (4%) leads to weaker mechanical properties due to the increased likelihood of agglomeration and potential sites for crack initiation. The results of SEM imaging showed that the printed samples exhibit high-quality microstructures with well-bonded layers and beads. The samples show no delamination, lack of fusion, or fractures. However, the addition of carbon black nanoparticles increases the number and size of voids, leading to decreased printability due to the altered viscosity of the elastomer nanocomposite. The dispersion of CB nanoparticles in the printed elastomer samples is affected by the concentration of CB. At 1% CB, the nanoparticles are well-dispersed and show good adhesion to the matrix. However, as the CB content increases to 2%, minor agglomeration occurs, and at 4% CB, severe clustering of nanoparticles leads to hole formation and discontinuity, negatively impacting the mechanical properties of the samples. The SMP material used in this study, Vistamaxx 6202, can be programmed at room temperature

through strain, offering high strain recovery and stretchability, but it has limitations, including immediate relaxation and low shape fixity. The mechanical properties of shape memory samples undergo significant changes after multiple shape memory cycles, with a notable drop in properties after the first cycle. The samples approach a steady state of mechanical properties after several cycles. The addition of CB can significantly improve the mechanical properties of shape memory elastomers by reducing the decline in properties after multiple cycles. CB reinforcement enables the samples to achieve a steady state more quickly and at higher stress levels with less drop. 4D printed elastomer that can be used as artificial muscles has been developed, inspired by the chameleon's tongue, to lift objects. The artificial muscles were created by cold programming the samples at room temperature and then using a heat gun to heat them and recover their original shape, lifting the object. The 4D-printed artificial muscles were able to lift objects of varying weights, including a table tennis ball and even a table tennis racket. The muscles were able to achieve strains of up to 148% and 86% for pure elastomer and elastomer nanocomposite, respectively.

Author Contributions

Abbas Bayati: conceptualization (lead), data curation (lead), investigation (lead), methodology (lead), validation (lead), writing – original draft (lead). **Davood Rahmatabadi:** conceptualization (equal), data curation (equal), formal analysis (equal), investigation (equal), methodology (equal), supervision (equal), writing – review and editing (equal). **Mahdi Khajepour:** data curation (supporting), formal analysis (supporting), writing – review and editing (supporting). **Majid Baniassadi:** formal analysis (supporting), investigation (supporting), methodology (supporting), supervision (supporting), writing – review and editing (supporting). **Karen Abrinia:** formal analysis (supporting), investigation (supporting), methodology (supporting), supervision (supporting), writing – review and editing (supporting). **Mahdi Bodaghi:** conceptualization (supporting), formal analysis (supporting), investigation (equal), methodology (equal), supervision (equal), writing – review and editing (lead). **Mostafa Baghani:** formal analysis (supporting), investigation (equal), methodology (equal), supervision (lead), writing – review and editing (supporting).

Conflicts of Interest

The authors declare no conflicts of interest.

Data Availability Statement

The data that support the findings of this study are available from the corresponding author upon reasonable request.

References

1. K. P. Liles, A. F. Greene, M. K. Danielson, et al., "Photoredox-Based Actuation of an Artificial Molecular Muscle," *Macromolecular Rapid Communications* 39, no. 17 (2018): 1700781, https://doi.org/10.1002/marc.201700781.

2. J. C. Ince, A. R. Duffy, and N. V. Salim, "Macromolecular Rapid Communications," 45 (2024): 2400370.

3. G. Zhao, Z. Sun, D. Qiao, J. Yang, A. R. Chatto, and H. Wang, "Fabrication and Applied Investigation of a Muscle-Like Linear Actuator Using Ionic Polymer Metal Composites," *Polymer Composites* 38, no. 1 (2017): 147–156.

4. F. Wang, Q. Zhou, S. Zheng, Q. Li, and S. Park, "High-Performance Carboxylated Cellulose Nanofibers-Based Electro-Responsive Ionic Artificial Muscles Toward Bioinspired Applications," *Polymer Composites* 45 (2024): 10365–10374.

5. S. M. Mirvakili and I. W. Hunter, "Artificial Muscles: Mechanisms, Applications, and Challenges," *Advanced Materials* 30 (2018): 1704407.

6. M. Duduta, E. Hajiesmaili, H. Zhao, R. J. Wood, and D. R. Clarke, "Realizing the Potential of Dielectric Elastomer Artificial Muscles," *Proceedings of the National Academy of Sciences of the United States of America* 116 (2019): 2476–2481.

7. B. Tondu and P. Lopez, "Modeling and Control of McKibben Artificial Muscle Robot Actuators," *IEEE Control Systems* 20 (2000): 15–38.

8. M. A. Meller, M. Bryant, and E. Garcia, "Reconsidering the McKibben Muscle: Energetics, Operating Fluid, and Bladder Material," *Journal of Intelligent Material Systems and Structures* 25, no. 18 (2014): 2276–2293, https://doi.org/10.1177/1045389X14549872.

9. F. Daerden and D. Lefeber, "Pneumatic Artificial Muscles: Actuators for Robotics and Automation," *European Journal of Mechanical and Environmental Engineering* 47 (2002): 11.

10. K. C. Wickramatunge and T. Leephakpreeda, "Study on Mechanical Behaviors of Pneumatic Artificial Muscle," *International Journal of Engineering Science* 48 (2010): 188–198.

11. J. J. Misuraca and C. Mavroidls, *Proceedings of the ASME 2022 International Mechanical Engineering Congress and Exposition (IMECE 2022)*, vol. 2 (ASME, 2021), 963.

12. B. Tondu, V. Boitier, and P. Lopez, "Naturally Compliant Robot-Arms Actuated by Mckibben Artificial Muscles," in *Proceedings of IEEE International Conference on Systems, Man and Cybernetics*, vol. 3 (IEEE, 1994), 2635–2640.

13. M. Joyce, T. Hodgkinson, M. Lemoine, A. González-Vázquez, D. J. Kelly, and F. J. O'Brien, "Development of a 3D-Printed Bioabsorbable Composite Scaffold With Mechanical Properties Suitable for Treating Large, Load-Bearingarticular Cartilage Defects," *European Cells & Materials* 45 (2023): 158–172, https://doi.org/10.22203/eCM.v045a11.

14. B. Kalita, A. Leonessa, and S. K. Dwivedy, "A Review on the Development of Pneumatic Artificial Muscle Actuators: Force Model and Application," *Actuators* 11 (2022): 288.

15. D. Kongahage, A. Ruhparwar, and J. Foroughi, "High Performance Artificial Muscles to Engineer a Ventricular Cardiac Assist Device and Future Perspectives of a Cardiac Sleeve," *Advanced Materials Technologies* 6 (2021): 2000894.

16. Y. Wang, K. Uesugi, T. Nitta, Y. Hiratsuka, and K. Morishima, "Contractile and Tensile Measurement of Molecular Artificial Muscles for Biohybrid Robotics," *Cyborg and Bionic Systems* 5 (2024): 5.

17. C. A. M. La Porta, M. C. Lionetti, S. Bonfanti, et al., "Metamaterial Architecture From a Self-Shaping Carnivorous Plant," *Proceedings of the National Academy of Sciences of the United States of America* 116 (2019): 18777–18782.

18. D. Rahmatabadi, M. Khajepour, A. Bayati, et al., "Advancing Sustainable Shape Memory Polymers Through 4D Printing of Polylactic Acid-Polybutylene Adipate Terephthalate Blends," *European Polymer Journal* 216 (2024): 113289.

19. M. Yang, Y. Xu, X. Xin, et al., "4D Printed Cardiac Occlusion Device With Efficient Anticoagulation, Proendothelialization, and Precise Localization," *Advanced Functional Materials* (2025): 2412533.

20. M. Nejatpour, A. Fallah, and B. Koc, "An Overview of 4D Printing of Smart Multifunction Continuous Fiber-Reinforced Composites: Recent Advances and Novel Applications," *Advanced Composites and Hybrid Materials* 7 (2024): 133.

21. X. Huang, K. Kumar, M. K. Jawed, et al., "Highly Dynamic Shape Memory Alloy Actuator for Fast Moving Soft Robots," *Advanced Materials Technologies* 4 (2019): 1800540.

22. G. Singh Rajput, J. Vora, P. Prajapati, and R. Chaudhari, "Areas of Recent Developments for Shape Memory Alloy: A Review," *Materials Today Proceedings* 62 (2022): 7194–7198.

23. A. Price, A. Edgerton, C. Cocaud, H. Naguib, and A. Jnifene, "A Study on the Thermomechanical Properties of Shape Memory Alloys-Based Actuators Used in Artificial Muscles," *Journal of Intelligent Material Systems and Structures* 18 (2007): 11–18, https://doi.org/10.1177/1045389X06064000.

24. H. B. Park, D. R. Kim, H. J. Kim, W. Wang, M. W. Han, and S. H. Ahn, "Design and Analysis of Artificial Muscle Robotic Elbow Joint Using Shape Memory Alloy Actuator," *International Journal of Precision Engineering and Manufacturing* 21, no. 2 (2020): 249–256, https://doi.org/10.1007/s12541-019-00240-8.

25. Y. Chen, C. Chen, H. U. Rehman, et al., "Shape-Memory Polymeric Artificial Muscles: Mechanisms, Applications and Challenges," *Molecules* 25 (2020): 4246.

26. W. M. Huang, Z. Ding, C. C. Wang, J. Wei, Y. Zhao, and H. Purnawali, "Shape Memory Materials," *Materials Today* 13 (2010): 54–61.

27. M. Baniasadi, E. Yarali, M. Bodaghi, A. Zolfagharian, and M. Baghani, "Constitutive Modeling of Multi-Stimuli-Responsive Shape Memory Polymers With Multi-Functional Capabilities," *International Journal of Mechanical Sciences* 192 (2021): 106082.

28. D. Rahmatabadi, M. Aberoumand, K. Soltanmohammadi, et al., "A New Strategy for Achieving Shape Memory Effects in 4D Printed Two-Layer Composite Structures," *Polymers* 14, no. 24 (2022): 5446, https://doi.org/10.3390/polym14245446.

29. X. Zuo, Y. Zhou, K. Hao, et al., "3D Printed All-Natural Hydrogels: Flame-Retardant Materials Toward Attaining Green Sustainability," *Advancement of Science* 11 (2024): 2306360.

30. Q. He, Z. Wang, Z. Song, and S. Cai, "Bioinspired Design of Vascular Artificial Muscle," *Advanced Materials Technologies* 4 (2019): 1800244.

31. P. Honari, D. Rahmatabadi, A. Bayati, et al., "Simultaneous 4D Printing and In-Situ Foaming for Tailoring Shape Memory Behaviors in Polylactic Acid Foams," *Manufacturing Letters* 43 (2025): 33–36.

32. M. Hashimoto, T. Sato, and Y. Taguchi, "Additive Manufacturing Method of Electrothermal 4D Bimorph Microactuator," *Sensors and Actuators A: Physical* 356 (2023): 114348, https://doi.org/10.1016/j.sna.2023.114348.

33. H. A. Colorado, E. I. Gutierrez-Velasquez, L. D. Gil, and I. L. de Camargo, "Exploring the Advantages and Applications of Nanocomposites Produced via Vat Photopolymerization in Additive Manufacturing: A Review," *Advanced Composites and Hybrid Materials* 7, no. 1 (2024): 1, https://doi.org/10.1007/s42114-023-00808-z.

34. Y. Xu, F. Zhang, W. Zhai, S. Cheng, J. Li, and Y. Wang, "Unraveling of Advances in 3D-Printed Polymer-Based Bone Scaffolds," *Polymers (Basel)* 14 (2022): 566.

35. D. Rahmatabadi, K. Soltanmohammadi, M. Aberoumand, et al., "4D Printing of Porous PLA-TPU Structures: Effect of Applied Deformation, Loading Mode and Infill Pattern on the Shape Memory Performance," *Physica Scripta* 99 (2024): 025013.

36. A. Sun, S. Ma, X. Shi, et al., "4D Printing of Temperature-Responsive Composites With Programmable Thermochromic Deformation Bifunctional," *Sensors and Actuators A: Physical* 368 (2024): 115138, https://doi.org/10.1016/j.sna.2024.115138.

37. M. A. Yousefi, D. Rahmatabadi, M. Baniassadi, M. Bodaghi, and M. Baghani, "4D Printing of Multifunctional and Biodegradable PLA-PBAT-Fe_3O_4 Nanocomposites With Supreme Mechanical and Shape Memory Properties," *Macromolecular Rapid Communications* 46, no. 2 (2024): 2400661, https://doi.org/10.1002/marc.202400661.

38. M. López-Valdeolivas, D. Liu, D. J. Broer, et al., "4D Printed Actuators With Soft-Robotic Functions," *Macromolecular Rapid Communications* 39, no. 5 (2018): 1700710, https://doi.org/10.1002/marc.201700710.

39. S. E. Bakarich, R. Gorkin, and G. M. Spinks, "4D Printing With Mechanically Robust, Thermally Actuating Hydrogels," *Macromolecular Rapid Communications* 36, no. 12 (2015): 1211–1217, https://doi.org/10.1002/marc.201500079.

40. M. Lalegani Dezaki and M. Bodaghi, "Shape Memory Meta-Laminar Jamming Actuators Fabricated by 4D Printing," *Soft Materials* 19 (2023): 2186–2203.

41. E. Zhang, T. Pang, Y. Zhang, et al., "Fully 3D Printed Dielectric Elastomer Actuators Based on Silicone and its Composites," *Polymer Composites* 45 (2024): 12159–12171.

42. S. Kumar, N. Ojha, M. R. Ramesh, and M. Doddamani, "Polymer Composites," 2024.

43. M. Aberoumand, D. Rahmatabadi, K. Soltanmohammadi, et al., "Stress Recovery and Stress Relaxation Behaviors of PVC 4D Printed by FDM Technology for High-Performance Actuation Applications," *Sensors and Actuators A: Physical* 361 (2023): 114572.

44. Y. Yang, Y. Wu, C. Li, X. Yang, and W. Chen, "Flexible Actuators for Soft Robotics," *Advanced Intelligent Systems* 2 (2020): 1900077.

45. M. H. Mahmoudinezhad, I. Anderson, and S. Rosset, "Interdigitated Sensor Based on a Silicone Foam for Subtle Robotic Manipulation," *Macromolecular Rapid Communications* 42 (2021): 2000560.

46. M. Kalulu, B. Chilikwazi, J. Hu, and G. Fu, "Soft Actuators and Actuation: Design, Synthesis, and Applications," *Macromolecular Rapid Communications* 46, no. 7 (2024): 2400282, https://doi.org/10.1002/marc.202400282.

47. J. Cai, A. Vanhorn, C. Mullikin, J. Stabach, Z. Alderman, and W. Zhou, "4D Printing of Soft Robotic Facial Muscles," 2015.

48. B. Sparrman, C. du Pasquier, C. Thomsen, et al., "Printed Silicone Pneumatic Actuators for Soft Robotics," *Additive Manufacturing* 40 (2021): 101860.

49. D. J. Roach, C. Yuan, X. Kuang, et al., "Long Liquid Crystal Elastomer Fibers With Large Reversible Actuation Strains for Smart Textiles and Artificial Muscles," *ACS Applied Materials & Interfaces* 11, no. 21 (2019): 19514–19521, https://doi.org/10.1021/acsami.9b04401.

50. A. Bayati, D. Rahmatabadi, I. Ghasemi, et al., "3D Printing Super Stretchable Propylene-Based Elastomer," *Materials Letters* 361 (2024): 136075.

51. M. A. Munir, F. Rahmawati, J. A. Jamal, et al., "Fabrication and Characterization of New Bio-Based Electrode Polyurethane: Diverse Conducting Materials Impacts Such as Graphene Oxide, Gold, and Carbon Nanotube," *Green Chemistry Letters and Reviews* 17 (2024): 17.

52. M. A. Munir, K. H. Badri, L. Y. Heng, et al., "Design and Synthesis of Conducting Polymer Bio-Based Polyurethane Produced From Palm Kernel Oil," *International Journal of Polymeric Science* 2022 (2022): 6815187.

53. A. Karimi, D. Rahmatabadi, and M. Baghani, "Direct Pellet Three-Dimensional Printing of Polybutylene Adipate-Co-Terephthalate for a Greener Future," *Polymers* 16 (2024): 267.

54. E. L. Gilmer, D. Miller, C. A. Chatham, et al., "Model Analysis of Feedstock Behavior in Fused Filament Fabrication: Enabling Rapid Materials Screening," *Polymer (Guildford)* 152 (2018): 51–61, https://doi.org/10.1016/j.polymer.2017.11.068.

55. N. A. Patil, K. Joshi, J. Lee, et al., "Additive Manufacturing of Thermoplastic Elastomer Structures Using Dual Material Core-Shell Filaments," *Additive Manufacturing* 82 (2024): 104044.

56. E. Soleyman, D. Rahmatabadi, K. Soltanmohammadi, et al., "Shape Memory Performance of PETG 4D Printed Parts Under Compression in

Cold, Warm, and Hot Programming," *Smart Materials and Structures* 31 (2022): 085002.

57. S. Zhu, J. Hu, and Y. Zhang, "A Single Polymer Artificial Muscle Having Dual-Mode Contractibility, Temperature Sensibility, and Trainability Through Enthalpy Change," *Advanced Materials Technologies* 4 (2019): 1900017.

58. A. Kotikian, R. L. Truby, J. W. Boley, T. J. White, and J. A. Lewis, "3D Printing of Liquid Crystal Elastomeric Actuators With Spatially Programed Nematic Order," *Advanced Materials* 30 (2018): 1706164.

59. C. S. Haines, M. D. Lima, N. Li, et al., "Artificial Muscles From Fishing Line and Sewing Thread," *Science* 343, no. 6173 (2014): 868–872, https://doi.org/10.1126/science.1246906.

60. C. S. Haines, N. Li, G. M. Spinks, A. E. Aliev, J. Di, and R. H. Baughman, "New Twist on Artificial Muscles," *Proceedings of the National Academy of Sciences* 113 (2016): 11709–11716.

61. J. H. De Groot and J. L. Van Leeuwen, "Evidence for an Elastic Projection Mechanism in the Chameleon Tongue," *Proceedings of the Royal Society B: Biological Sciences* 271, no. 1540 (2004): 761–770, https://doi.org/10.1098/rspb.2003.2637.

62. A. Herrel, J. J. Meyers, P. Aerts, and K. C. Nishikawa, "Functional Implications of Supercontracting Muscle in the Chameleon Tongue Retractors," *Journal of Experimental Biology* 204 (2001): 3621–3627.

63. F. Brau, D. Lanterbecq, L. N. Zghikh, V. Bels, and P. Damman, "Dynamics of Prey Prehension by Chameleons Through Viscous Adhesion," *Nature Physics* 12, no. 10 (2016): 931–935, https://doi.org/10.1038/nphys3795.

64. C. G. Robertson and N. J. Hardman, "Nature of Carbon Black Reinforcement of Rubber: Perspective on the Original Polymer Nanocomposite," *Polymers (Basel)* 13, no. 4 (2021): 538, https://doi.org/10.3390/polym13040538.

65. M. Sahihi and F. Bedoui, *Nano-Reinforced Polymers and Polymer Nanocomposites* (Springer Nature Singapore, 2024), 267.

66. Y. A. El-Shekeil, F. M. AL-Oqla, H. A. Refaey, S. Bendoukha, and N. Barhoumi, "Investigating the Mechanical Performance and Characteristics of Nitrile Butadiene Rubber Date Palm Fiber Reinforced Composites for Sustainable Bio-Based Materials," *Journal of Materials Research and Technology* 29 (2024): 101–108.

67. M. S. Goyat, A. Hooda, T. K. Gupta, et al., "Role of Non-Functionalized Oxide Nanoparticles on Mechanical Properties and Toughening Mechanisms of Epoxy Nanocomposites," *Ceramics International* 47 (2021): 22316–22344.

68. J. Turicek, E. Kowal, K. Holland, et al., "Effects of Porosity on the Mechanical Properties of Additively Manufactured Components: A Critical Review," *Materials Research Express* 7, no. 12 (2020): 122001, https://doi.org/10.1088/2053-1591/abcc5d.

69. Y. Tao, F. Kong, Z. Li, et al., "A Review on Voids of 3D Printed Parts by Fused Filament Fabrication," *Elsevier* 15 (2021): 4860.

70. C. Gupta, P. MB, N. K. Shet, A. K. Ghosh, S. Bandyopadhyay, and P. Mukhopadhyay, "Microstructure and Mechanical Performance Examination of 3D Printed Acrylonitrile Butadiene Styrene Thermoplastic Parts," *Polymer Engineering and Science* 60, no. 11 (2020): 2770–2781, https://doi.org/10.1002/pen.25507.

71. X. Sun, M. Mazur, and C. T. Cheng, "A Review of Void Reduction Strategies in Material Extrusion-Based Additive Manufacturing," *Additive Manufacturing* 67 (2023): 103463.

72. J. Wang, Y. Li, D. Zheng, H. Mikulčić, M. Vujanović, and B. Sundén, "Preparation and Thermophysical Property Analysis of Nanocomposite Phase Change Materials for Energy Storage," *Renewable and Sustainable Energy Reviews* 151 (2021): 111541.

73. D. Rahmatabadi, A. Bayati, M. Khajepour, et al., "Poly(Ethylene Terephthalate) Glycol/Carbon Black Composites for 4D Printing," *Materials Chemistry and Physics* 325 (2024): 129737.

74. E. G. Karvelas, N. K. Lampropoulos, L. T. Benos, T. Karakasidis, and I. E. Sarris, "On the Magnetic Aggregation of Fe_3O_4 Nanoparticles," *Computer Methods and Programs in Biomedicine* 198 (2021): 105778.

75. J. Guo, C. H. Tsou, Y. Yu, et al., "Conductivity and Mechanical Properties of Carbon Black-Reinforced Poly(Lactic Acid) (PLA/CB) Composites," *Iranian Polymer Journal (English Ed.)* 30, no. 12 (2021): 1251–1262, https://doi.org/10.1007/s13726-021-00973-2.

76. D. Rahmatabadi, M. Aberoumand, K. Soltanmohammadi, et al., "Toughening PVC With Biocompatible PCL Softeners for Supreme Mechanical Properties, Morphology, Shape Memory Effects, and FFF Printability," *Macromolecular Materials and Engineering* 308 (2023): 2300114.

77. M. Cvek, M. Kracalik, M. Sedlacik, M. Mrlik, and V. Sedlarik, "Reprocessing of Injection-Molded Magnetorheological Elastomers Based on TPE Matrix," *Composites. Part B, Engineering* 172 (2019): 253–261.

78. E. Ghobadi, A. Shutov, and H. Steeb, "Parameter Identification and Validation of Shape-Memory Polymers Within the Framework of Finite Strain Viscoelasticity," *Materials* 14, no. 8 (2021): 2049, https://doi.org/10.3390/ma14082049.

79. D. Gutierrez-Lemini, "Eng. Viscoelasticity," (2014): 1.

80. J. D. Ferry, *Viscoelastic Properties of Polymers*, vol. 264 (Wiley, 1980).

81. Z. Liao, J. Yang, M. Hossain, G. Chagnon, and X. Yao, "The Time and Temperature Dependences of the Stress Recovery of Ecoflex Polymer," *International Journal of Non-Linear Mechanics* 149 (2023): 104338, https://doi.org/10.1016/j.ijnonlinmec.2022.104338.

82. Z. Tu, W. Liu, J. Wang, et al., "Biomimetic High Performance Artificial Muscle Built on Sacrificial Coordination Network and Mechanical Training Process," *Nature Communications* 12 (2021): 1.

83. M. Rogóż, J. Haberko, and P. Wasylczyk, "Light-Driven Linear Inchworm Motor Based on Liquid Crystal Elastomer Actuators Fabricated With Rubbing Overwriting," *Materials (Basel)* 14 (2021): 6688.

84. J. Shu, D. A. Ge, E. Wang, et al., "A Liquid Metal Artificial Muscle," *Advanced Materials* 33, no. 43 (2021): 2103062, https://doi.org/10.1002/adma.202103062.

85. J. Sun, B. Tighe, Y. Liu, and J. Zhao, "Twisted-and-Coiled Actuators With Free Strokes Enable Soft Robots With Programmable Motions," *Soft Robotics* 8, no. 2 (2021): 213–225, https://home.liebertpub.com/soro.

86. M. Li, Y. Tang, R. H. Soon, B. Dong, W. Hu, and M. Sitti, "Miniature Coiled Artificial Muscle for Wireless Soft Medical Devices," *Science Advances* 8 (2022): 5616.

87. D. Xie, Z. Ma, J. Liu, and S. Zuo, "Pneumatic Artificial Muscle Based on Novel Winding Method," *Actuators* 10 (2021): 100.

88. W. Kim, H. Park, and J. Kim, "Compact Flat Fabric Pneumatic Artificial Muscle (ffPAM) for Soft Wearable Robotic Devices," *IEEE Robotics and Automation Letters* 6, no. 2 (2021): 2603–2610, https://doi.org/10.1109/LRA.2021.3062012.

89. Y. Liu, S. Yue, Z. Tian, et al., "Self-Powered and Self-Healable Extraocular-Muscle-Like Actuator Based on Dielectric Elastomer Actuator and Triboelectric Nanogenerator," *Advanced Materials* 36, no. 7 (2024): 2309893, https://doi.org/10.1002/adma.202309893.

90. Q. He, Z. Wang, Y. Wang, et al., "Electrospun Liquid Crystal Elastomer Microfiber Actuator," *Science Robotics* 6, no. 57 (2021): eabi9704, https://doi.org/10.1126/scirobotics.abi9704.

Supporting Information

Additional supporting information can be found online in the Supporting Information section.